Luminescent probe synthesis for oxygen visualization technique: Application to the effect of surfactant structure on oxygen mass transfer

Gaëlle Lebrun, Bilal El Mokdad, Claude Le Men, Véronique Pimienta, Christophe Coudret, Clément Roux, Gilles Hébrard, Nicolas Dietrich

LUMINESCENT PROBE SYNTHESIS FOR OXYGEN VISUALIZATION TECHNIQUE: APPLICATION TO THE EFFECT OF SURFACTANT STRUCTURE ON OXYGEN MASS TRANSFER

Gaëlle Lebrun[1,3], Bilal El Mokdad[1,3], Claude Le Men[1,3], Véronique Pimienta[2,3], Christophe Coudret[2,3], Clément Roux[2,3], Gilles Hébrard[1,3], Nicolas Dietrich[1,3,*]

[1] Toulouse Biotechnology Institute (TBI), Université de Toulouse, CNRS, INRAE, INSA, Toulouse, France

[2] Laboratoire des IMRCP, Université de Toulouse, CNRS UMR 5623, Université Paul Sabatier, Toulouse, France

[3]Fédération de recherche FERMAT, CNRS, 31000 Toulouse, France

*Corresponding author: dietrich@insa-toulouse.fr (N. Dietrich)

Abstract

Planar Laser Induced Fluorescence with Inhibition (PLIF-I) is a powerful technique for studying the local gas/liquid oxygen mass transfer from a single rising bubble. However, to track oxygen in the liquid phase, it is necessary to use an oxygen sensitive luminescent probe, which needs to be unreactive toward the liquid phase. This article presents the synthesis of a fluorophore, $[Ru(dpp\text{-}diSO_3)_3]Na_4$, to be used in liquid phases containing anionic molecules. To avoid electrostatic interactions, the fluorophore and the component present in the liquid phase need to have the same charge. Thanks to the use of this new luminescent probe in PLIF-I application, the influence of the chain length of anionic surfactants (dodecyl sulfate sodium salt and tetradecyl sulfate sodium salt) on oxygen mass transfer has been studied at different concentrations (1.3×10^{-3}-2.5×10^{-7} mol.L^{-1}). Results show that, for a given bulk concentration, the longer the hydrophobic chain, the greater the decrease in velocity and mass transfer coefficient. These results are compared with those of a previous paper dealing with length of cationic and nonionic surfactants and a correlation is proposed, taking account of the intrinsic properties of surfactants and their concentration in the liquid phase.

Keywords

PLIF-I, fluorescence quenching, surfactants, oxygen transfer, gas/liquid interface, adsorption

1 Introduction

Mass transfer at gas-liquid interfaces is of great interest in many industrial applications [1,2], such as chemical and biological processes, and in environmental systems. For wastewater treatment, the water aeration through air bubbles is determinant for the efficiency of pollutant degradation [3]. The high industrial demand concerning decreases of power consumption during the aeration step led to intensive studies about mass transfer in gas-liquid contactors, but this issue becomes more complex in the presence of contaminants, especially surfactants, which are amphiphilic molecules, coming from all kinds of domestic detergents, and are also excreted by microorganisms present in wastewater treatment plants. As a result, surfactants are found in a large amounts in wastewater and predicting mass transfer in such configurations requires a good understanding of all the phenomena occurring during mass transfer in the presence of contaminants.

If the medium in which the bubble rises contains surfactants, this has an impact on the hydrodynamic parameters of the bubble, such as shape, velocity and interfacial area, [4–6]. The velocity of the bubble is a key parameter in mass transfer phenomena because it affects (i) the residence time of the bubble in the liquid phase and also (ii) buoyancy at the vicinity of the interface. As has been described by Palaparthi et al. [7], surfactants adsorb to the bubble surface and are swept from the nose to the rear of the bubble. The resulting high local concentration at the rear leads to a desorption of surfactants. A surface tension gradient appears between the nose and the rear of the bubble and leads to the appearance of a Marangoni flow, which opposes the advection flow and slows the bubble down. From this description of bubble contamination, the bubble can be split in two regions [8]: at its nose, the bubble is clean and the flows satisfy slip conditions, while the rear of the bubble is fully contaminated and the interfacial velocity drops to zero. A contamination angle θ_{cap} can be used to describe the level of contamination of the rear of the bubble. Sadhal and Johnson [8] proposed a calculation of this angle

from the drag force acting on the bubble, which is highly dependent on the contamination. The large majority of the literature conclude on a decrease of velocity and mass transfer coefficient in the presence of surfactants, however it can be underlined that Àlvarez et al. and Gómez-Díaz et al. that at very low surfactant concentration, mass transfer can be enhanced thanks to the buoyancy created by Marangoni flow [9,10].

Taking this molecular consideration of bubble colonization by surfactants into account, numerous experimental studies have investigated mass transfer from a contactor point of view [11–15]. The study of bubble columns brings us closer to an industrial application. However, because of the numerous events taking place in the column at the same time (coalescence, breakage), and measurement of an averaged mass transfer in the whole column , it is sometimes difficult to identify and isolate mechanisms involved in mass transfer. Some research works have pointed out that some additional resistance having a physicochemical source should be taken into account [13,14,16,17]. In response to this interrogation, local scale studies are necessary to investigate mechanisms that occur during mass transfer. This local scale can be reached by Direct Numerical Simulation (DNS), which is a powerful tool to investigate the local distribution of surfactants around the bubble and thus gain access to a better understanding of their link with hydrodynamics and physicochemical phenomena close to the interface [18–21]. From an experimental point of view, few techniques for direct visualization of mass transfer have been developed. These techniques use a fluorophore or colored molecule as the oxygen [20,22–28] or carbon dioxide [29–36] sensor. Among these techniques, Planar Laser Induced Fluorescence with Inhibition (PLIF-I) enables measurements of mass transfer from a single bubble rising in a quiescent liquid [37–43] and provides access to (i) its shape, velocity, and diameter, and (ii) the oxygen mass transfer coefficient and diffusion coefficient in the liquid phase, with good precision. This very powerful technique then allows hydrodynamic and mass transfer to be uncoupled. They are both knew with good precision, which makes it a very good technique for investigating mechanisms of oxygen transfer in the presence of surfactants.

In recent decades, numerous studies have shown the strong impact of the structure of surfactants and their properties on the mass transfer coefficient. Jia et al. [44] demonstrated that mass transfer coefficient

decreases with decreasing Critical Micellar Concentration (CMC). The charge of the head has been demonstrated to have an impact on the mass transfer coefficient [14,45,46]. Garcia-Aubuin et al. [47] showed that, the longer the hydrophobic chain length of cationic surfactant is, the more the mass transfer coefficient decreases. Similar results highlighted in our previous study [48], conducted with the PLIF-I technique, showed that the length of the tail of cationic surfactants has a strong impact on the oxygen mass transfer coefficient, although the hydrophilic length of nonionic surfactants does not impact mass transfer for a given bulk concentration. This previous study could not conclude on the effect of anionic surfactant length because the fluorophore used as the oxygen tracer interacted with anionic surfactants.

This study proposes a luminescent probe for use in the PLIF-I technique; $[Ru(dpp\text{-}diSO_3)_3]Na_4$, in order to make possible the use of this technique in the presence of anionic surfactants. This paper will first present the synthesis of this fluorescent molecule, and characterize its fluorescence properties. Then, its use as an oxygen sensor in the PLIF-I technique will be validated in pure water conditions.

Once the use of $[Ru(dpp\text{-}diSO_3)_3]Na_4$ is validated in pure water, the study shows its compatibility with anionic surfactants, and presents results of PLIF-I experiments run with sodium dodecyl sulfate (SDS) and sodium tetradecyl sulfate (STS), which are anionic surfactants presenting the same polar head and hydrophobic chains of 12 and 14 carbons, respectively. This work is then compared with the results of Lebrun et al. [48] and the parameters that impact the mass transfer are investigated. Thus, a model correcting Higbie's [49] and Frössling's [50] correlations is proposed, by adding a new dimensionless parameter that describes the equilibrium between the surfactants adsorbed and in the bulk.

2 Material and method

2.1 Physico-chemistry

2.1.1 Surfactant solutions

All solutions were prepared with ultra-pure water having a conductivity of 0.054 $mS.cm^{-1}$. The surfactants chosen to study their effect on oxygen transfer were dodecyl sulfate sodium salt (SDS, CAS: 151-21-3, Sigma-Aldrich, USA) and tetradecyl sulfate sodium salt (STS, CAS: 1191-50-0, Sigma-

Aldrich, USA). Surfactant solutions were prepared at concentrations between 1.3×10^{-3} and 2.5×10^{-7} mol.L^{-1}. Surface tension of solutions was measured according to the Du Nouÿ ring method [51] (tensiometer: K6, Krüss, Germany).

2.1.2 Fluorophore synthesis

A fluorophore for the PLIF-I technique was synthetized in this work. The complex $[Ru(dpp\text{-}diSO_3]^{2-}$ has been selected, since it is known to exhibit O_2 sensing properties [52]. It was readily prepared using reported procedures but using microwave oven (Anton-Paar-300 monomode oven) heating [52,53] such as an oven is known to reduce side reactions and to accelerate the transformation [54,55]. The reagents used were Ruthenium (III) chloride, $RuCl_3.xH_2O$ (x: *ca* 6) (CAS: 10049-08-8, Sigma-Aldrich, USA), and the 2,7 bis-(sulfonatophenyl)- 1,10-phenanthroline sodium salt trihydrate (CAS:52746-49-3, Sigma-Aldrich, USA); they were used as received. The protocol followed was as follows: a solution of $RuCl_3.xH2O$ (113 mg, 0.546 mmol), 2,7 bis-(sulfonatophenyl)- 1,10-phenanthroline sodium salt trihydrate (1 g, 1.69 mmol) in argon-degassed ethylene glycol (20mL) was heated in a microwave oven for 2 hours at 220°C. After cooling, the dark orange reaction mixture was added to an excess of diethyl ether. The resulting precipitate was filtered then redissolved in a minimum amount of methanol before being applied in a reverse phase C18-column (ca 1x15cm) eluted with a MeOH: water mixture. Dark orange fractions were freeze dried. The yield obtained was 400 mg (42%).

2.2 Experimental setup

The experimental setup of Planar Laser Induced Fluorescence with Inhibition (PLIF-I) is depicted in Figure 1. It is composed of a column (1) (10x10x30 cm^3) filled with an aqueous solution. A millimetric single air bubble is generated in this solution through a needle 75 µm in internal diameter connected to a syringe pump, which can be activated remotely (Harvard apparatus PHD, 22/2000 Programmable, USA) (2). A CMOS camera (3) (Basler ace 12 bits, 1920x1200 $pixel^2$, Basler, Germany) was placed next to the column, and recorded the rise of the bubble at a rate of 250 $images.s^{-1}$ in a window of 1920x500 $pixel^{-1}$ at 20.31±0.04 $\mu m.pixel^{-1}$.

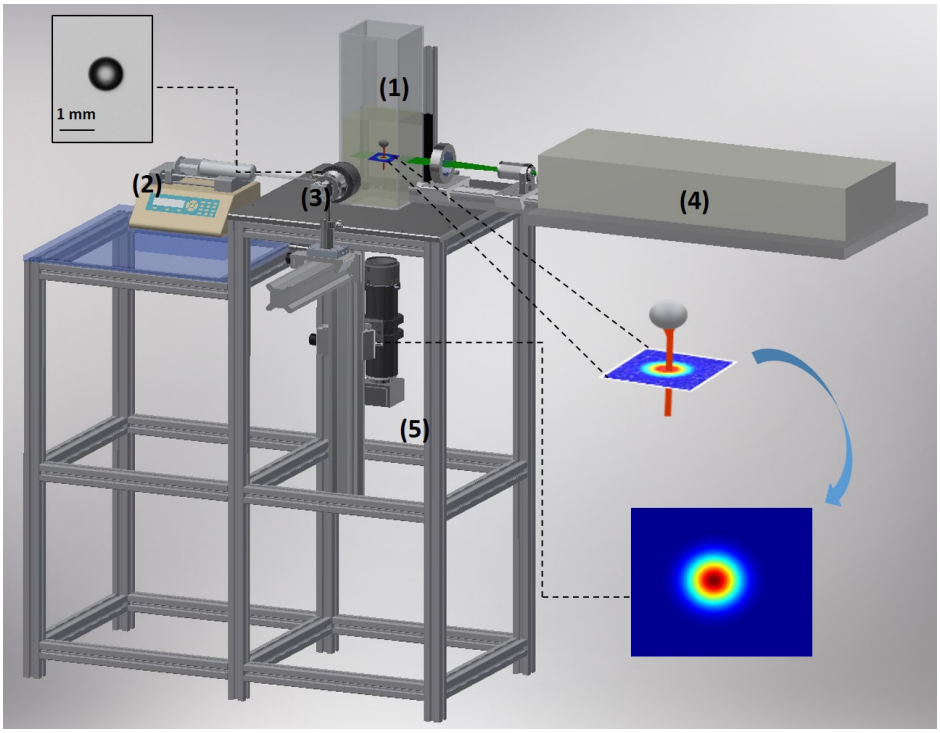

Figure 1: Experimental setup

This camera was positioned in such a way as to measure the diameter and velocity of the bubble; the viewing window was then around 39x10 mm^2 (the highest visualization axis in the vertical direction). The amount of oxygen transferred in the wake of the bubble was measured by fluorescence inhibition of a ruthenium complex. The ruthenium complex generally used is ruthenium dichlorotris(1,10-phenanthroline)ruthenium(II) hydrate (CAS: 20782-45-7, Sigma-Aldrich, USA), which is very suitable in the presence of non-charged or positively charged molecules. However, in order to perform measurements in the presence of anionic molecules, the ruthenium tris(diphenylphenanthroline disulfonate) sodium salt (CAS: 301206-84-8) was synthetized and will be more extensively described in the Results section. The fluorophore was then excited by a horizontal laser sheet (4) (Nd:YAG, laser: Dualpower 200-15, 15Hz, 2x200 mJ, Dantec Dynamics, Denmark) at 532 nm, in a plane perpendicular to the bubble wake, 50 mm above the injection point of the bubble (the bubble crossed this plane between 0.2 and 0.5 seconds after its generation, depending on its velocity). Fluorescence intensity was recorded by a CCD camera (5) (FlowSense, 12 bits, 2048x2048 pixels, Dantec Dynamics, Denmark) synchronized with the laser frequency and focused on the laser sheet. This camera was placed at the bottom of the column with a sampling rate of 4.37±0.04 $\mu m.pixel^{-1}$ (viewing window about 9x9 mm^2).

The camera was equipped with a 570 nm high pass filter. Before each experiment, a calibration curve was built by using an optical oxygen probe (multimeter: HQ40D, probe: Intellical LDO101, Hach, Germany) in order to determine the Stern Volmer [54] constants according to equation (1)

$$\frac{1}{G} = \frac{1}{G_0} + \frac{K_{sv}}{G_0}[O_2] \quad (1)$$

where G is the grey level, G_0 is the grey level in the absence of the quencher, $[O_2]$ mg.L^{-1} is the oxygen concentration and K_{sv} is the Stern Volmer constant (L.mg^{-1}). This calibration curve is built by injection of a mix of nitrogen and compressed air to obtain different concentration of oxygen. After mixing, the concentration of oxygen is supposed to be homogeneous and 100 images are taken from the bulk and related to an oxygen concentration, measured by the probe. To avoid spatial fluctuation, the calibration curve is built pixel by pixel. Once the calibration curve was applied to the images obtained in the bubble wake, the oxygen concentration was displayed on each pixel.

It was assumed that, far from the bubble, in its wake, convection could be neglected and all the matter motion was due only to diffusion of oxygen in the plane perpendicular to the bubble wake [37,38,41,48]. In previous studies [38,56], it was observed that, for spherical and quasi-spherical bubbles, the diffusion spot was circular and presented a Gaussian profile. As a result, it was possible to fit the oxygen field by equation (2), where the concentration $[O_2]$ in each pixel x_p, y_p was estimated.

$$[O_2](x,y) = Aexp\frac{-(x_p-X)^2+(y_p-Y)^2}{B} + C \quad (2)$$

Parameters were found by fitting the equation with the raw image using the "fminsearch" solver (Matlab R2017a). Note that A and B are parameters (mg.L^{-1} and pixel^2 respectively), and (X, Y) is the centre of the spot, the parameter C representing the background.

It was possible to calculate the flux of oxygen (mg.s^{-1}) transferred by the rising bubble with equation (3), where V_b is the velocity of the bubble (m.s^{-1}) measured by the side camera (3).

$$F_{O_2} = V_b \iint [O_2](x,y)dxdy \quad (3)$$

The mass transfer coefficient was then deduced from equation (4), where S_b is the surface area of the bubble, deduced from the equivalent diameter measured with the side camera (3); $[O_2]$ is the concentration at the beginning of the experiment (measured with the optical oxygen probe, close to 0 $mg.L^{-1}$); and $[O_2]^*$ is the saturation concentration of oxygen, also measured by the optical oxygen probe (close to 9.10 $mg.L^{-1}$).

$$k_L = \frac{F_{O_2}}{S_b([O_2]^* - [O_2])} \quad (4)$$

Finally, the diffusion coefficient of oxygen in the bulk was measured by a method developed by Xu et al. [40] assuming that the surface area of the spot S_{spot} increased with time following equation (5).

$$S_{spot} = 2\pi D_{O_2} \eta t \quad (5)$$

where η is a constant that can be fixed following the procedure described by Xu et al. [40]. Then the surface area of the spot was plotted versus time and the diffusion coefficient was extracted from the slope. Each condition was repeated 6 times in order to ensure the repeatability of measurements. All measurements were performed at room temperature (294±1K) and atmospheric pressure.

3 Results and discussion

3.1 Fluorophore synthesis

The goal was to synthetize a fluorescent molecule presenting (i) fluorescence inhibition in the presence of oxygen (ii) a negative global charge to avoid interaction with anionic molecules. This is made possible by using the sulfonated version of $[Ru(dpp)_3^{2+}]$ using disulfonato bathophenanthroline (dpp-diSO_3) instead of bathophenanthroline (dpp). The reaction between fluorescent complex (2,7 bis-(sulfonatophenyl)- 1,10-phenanthroline sodium salt trihydrate) and ruthenium ($RuCl_3$) is presented in Figure 2(a).

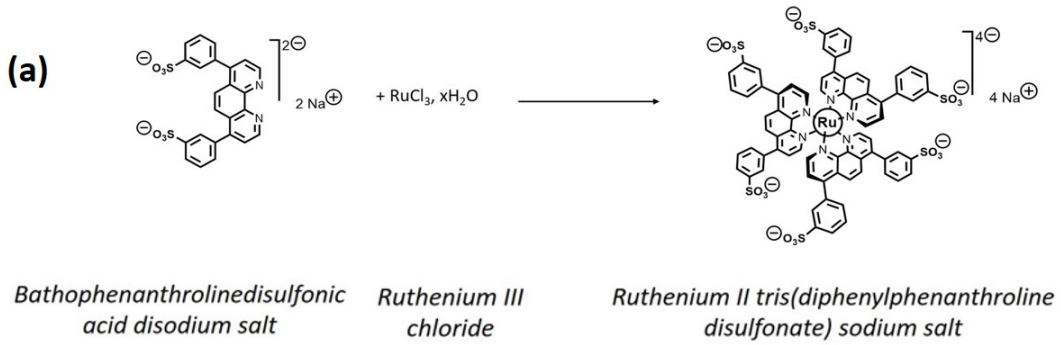

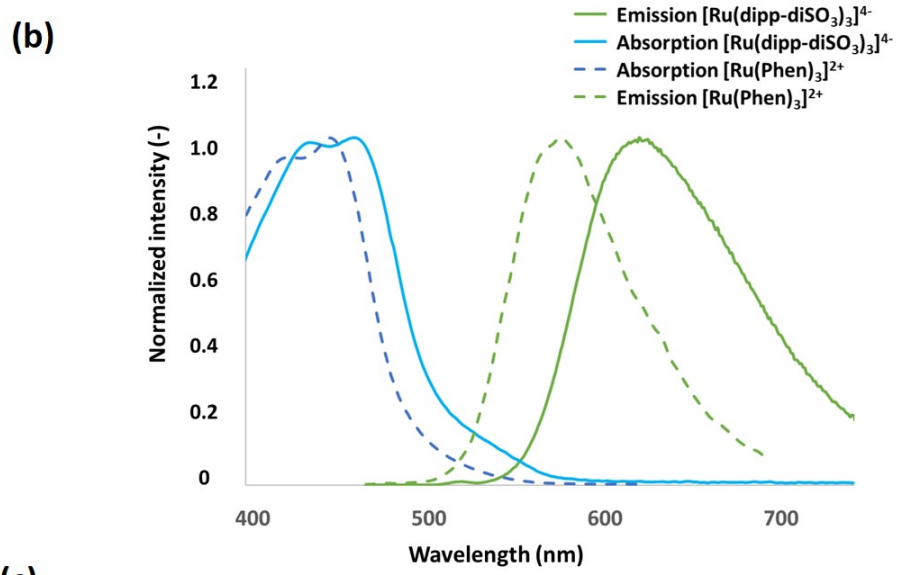

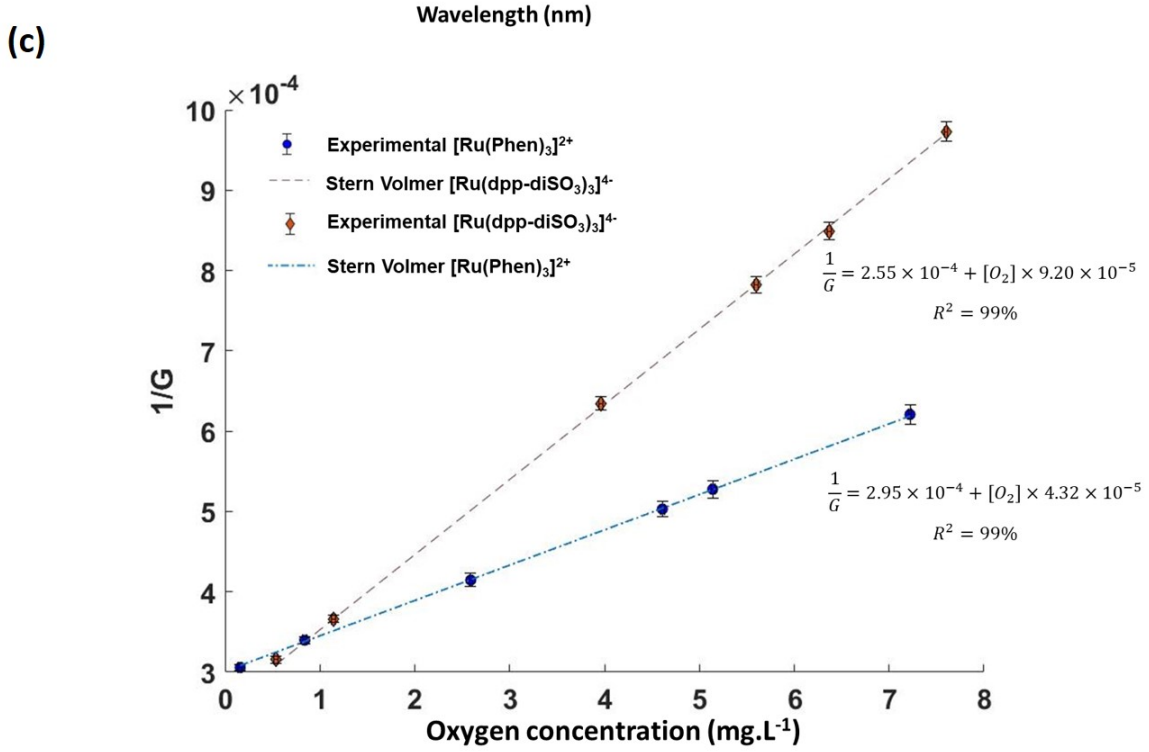

Figure 2: Fluorophore (a) synthesis (b) absorption/emission spectrum (b) calibration curve for PLIF-I experiments

In order to compare this new fluorophore with the conventional $[Ru(Phen)_3]^{2+}$ usually employed in PLIF-I experiments and only suitable for nonionic and cationic surfactants, the absorption-emission spectrum of both fluorophores are plotted and reported on the same graph, Figure 2(b). The maximum absorption wavelength was slightly higher in the case of $[Ru(dpp\text{-}diSO_3)_3]^{4-}$ (494 nm against 449 nm for $[Ru(Phen)_3]^{2+}$). In the same way, the maximal emission (absorption at 444nm) wavelength recorded was higher for $[Ru(dpp\text{-}diSO_3)_3]^{4-}$ than $[Ru(Phen)_3]^{2+}$. However, the two curves are close and this allows the fluorophore in the same experimental set-up conditions as used with $[Ru(Phen)_3]^{2+}$, presented in the Material and method section.

3.2 Fluorophore compatibility and mass transfer measurement

3.2.1 Fluorophore compatibility

Once the fluorescence properties of the $[Ru(dpp\text{-}diSO_3)_3]^{4-}$ had been verified, confirming that it could be used as an oxygen sensor in PLIF-I configuration, its fluorescence inhibition needed to follow the Stern Volmer law (equation (1)), with a Stern Volmer constant K_{sv} high enough to detect fluorescence fluctuation with variation of the oxygen concentration. A classical PLIF-I calibration curve was plotted with 70 $mg.L^{-1}$ of $[Ru(Phen)_3]^{2+}$ and compared with a calibration curve for 55 $mg.L^{-1}$ of our new fluorophore, $[Ru(dpp\text{-}diSO_3)_3]^{4-}$. The concentration of the fluorophore was chosen to be close to the concentration of $[Ru(Phen)_3]^{2+}$, usually preferred for PLIF-I experiments (70 $mg.L^{-1}$), and to use a minimum of product.

The two curves are presented in Figure 2(c) and are in good agreement with the Stern Volmer law (R^2=99%). Fluorescence inhibition by the oxygen was detected in both configurations. The important feature is the slope of the curve, which corresponds to the Stern Volmer Constant K_{sv}, as this constant expresses the ability of the oxygen to inhibit the fluorescence. As a result, the higher the constant is, the more the fluorescence is inhibited by oxygen, and thus, the easier it is to detect an oxygen variation. Concerning the new anionic fluorophore $[Ru(dpp\text{-}diSO_3)_3]^{4-}$, the constant found was $9.20.10^{-5}$ $L.mg^{-1}$,

the constant found for $[Ru(Phen)_3]^{2+}$ (the cationic fluorophore used previously) being $4.32.10^{-5}$ L.mg^{-1}. It is thus possible to conclude that the synthetized fluorophore was rather well inhibited by oxygen, and it would thus be possible to use it in the PLIF-I configuration to track the oxygen field in the presence of anionic surfactant.

Once the calibration curve had been plotted and the assumption that the fluorescence inhibition followed a Stern Volmer law with a high K_{sv} constant was validated, a PLIF-I experiment to measure oxygen transfer from a single millimetric bubble in pure water was run and compared with results obtained using $[Ru(Phen)_3]^{2+}$. The results are presented in Table 1.

Fluorophore	**$[Ru(Phen)_3]^{2+}$**	**$[Ru(dpp\text{-}diSO_3)_3]^{4-}$**
k_L (10^{-4} m.s^{-1})	5.7±0.5	5.2±0.2
D_{O2} (10^{-9} m^2.s^{-1})	2.0±0.1	2.0±0.1
d_{eq} (mm)	0.98±0.02	1.06±0.02
V_b (m.s^{-1})	0.267±0.007	0.274±0.008
Sh (=the detachment of bubbles $k_L d_{eq}/D_{O2}$)	269±21	275±15
Re (= $\rho d_{eq} V_b/\mu$)	263±8	289±9
Sc (= $\mu/(\rho D_{O2})$)	500±32	500±32

Table 1: Comparison between the PLIF-I results obtained in ultra-pure water with $[Ru(Phen)_3]^{2+}$ and $[Ru(dpp\text{-}diSO_3)_3]^{4-}$.

Table 1 presents hydrodynamic and oxygen transfer from a single isolated bubble. The second column gives results obtained in an aqueous solution of $[Ru(Phen)_3]^{2+}$ and the third column those found in an aqueous solution of $[Ru(dpp\text{-}diSO_3)_3]^{4-}$. The diameter and velocity of the bubbles generated are very close: diameter around 1 mm and resulting velocity around 270 mm.s^{-1}, as expected for a clean bubble of millimetric size [4]. The diffusion coefficient of oxygen is calculated from equation (5) (procedure described in the word of Xu et al. [40] with η=1) and is found to be the same in both solution (2.0×10^{-9} m^2.s^{-1}). Finally, the mass transfer coefficient and the Sherwood number are not significantly different,

and it is thus possible to conclude that the synthetized fluorophore $[Ru(dpp\text{-}diSO_3)_3]^{4-}$ can be used to track the oxygen transferred by bubbles to pure water solutions.

The ability of $[Ru(dpp\text{-}diSO_3)_3]^{4-}$ to serve as a good oxygen sensor in PLIF-I has been shown, but the compatibility with anionic molecules needs to be checked. For that purpose, measurements were made in a solution containing 2.95×10^{-5} mol.L^{-1} of SDS. An example of the results obtained is shown in Figure 3, where some raw images are presented versus time. The dark spot in the center of the image demonstrates the presence of oxygen. When the Stern Volmer calibration is applied to these images, the oxygen concentration field is obtained as shown in Figure 3 A and B. The signal to noise ratio is almost 100 at 0.20 seconds after the bubble's passage and 37 after 1.58 seconds. This ratio is good enough for the signal of interest to be clearly detected. The integral of this oxygen field corresponds to the total mass transferred in the plane perpendicular to the bubble wake. In the absence of vertical convection, this integral should be constant. This mass conservation is observed in Figure 3 on the graph representing the integral according to time, which is constant with a standard deviation of 2.5% over a period of 1.65 seconds. With the same protocol as described in Section 2, it is thus possible to determine the mass transfer coefficient of oxygen by the PLIF-I technique using $[Ru(dpp\text{-}diSO_3)_3]^{4-}$ as the oxygen probe.

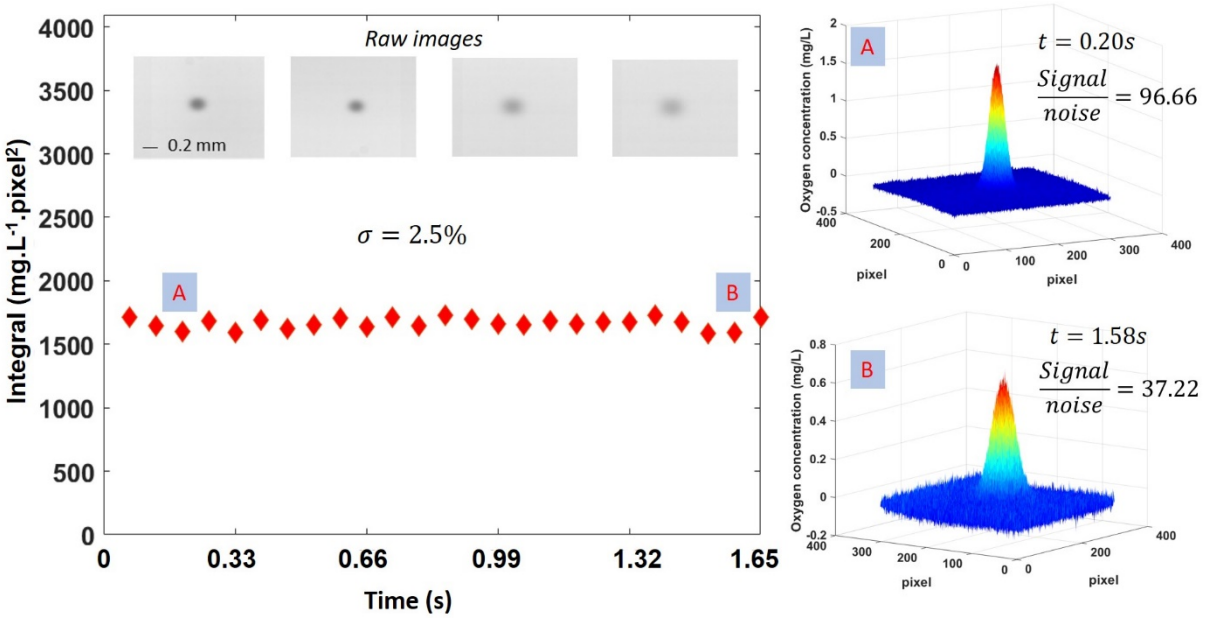

Figure 3: Example of oxygen field concentration obtained in the wake of a bubble rising in an aqueous solution of SDS

Finally, the PLIF-I technique allows the oxygen diffusion coefficient in the liquid phase to be determined by following the spreading of the surface spot with time. The figure presents the spreading of a surface inside the oxygen concentration field, in such a way that the mass in this surface area is constant. The linearity observed between the surface area and time gives access to the diffusion coefficient of oxygen. This linearity can be observed in Figure 4, and the diffusion coefficient in the SDS solution is then calculated to be 1.95×10^{-9} $m^2.s^{-1}$.

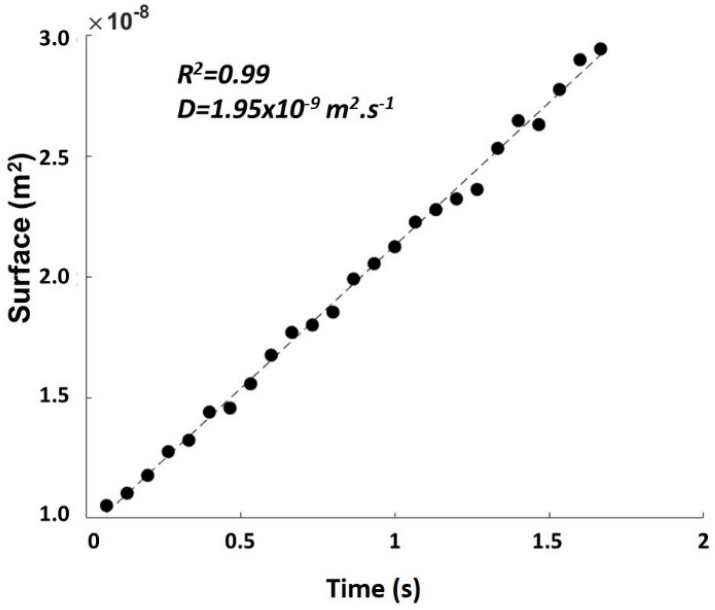

Figure 4: Expansion of the oxygen concentration field with time to measure diffusion coefficient of oxygen in an aqueous solution of SDS

3.2.2 Mass transfer measurements

The accuracy of $[Ru(dpp\text{-}diSO_3)_3]^{4-}$ as an oxygen probe in the presence of an anionic surfactant has been shown. This new fluorophore will be applied below to measure the mass transfer from a single, isolated bubble in the presence of anionic surfactants presenting different chain lengths and at different concentrations. The impact of the chain length of cationic and nonionic surfactants has been discussed in a previous paper [48] but it was not possible to consider the question in the presence of anionic surfactant due to the lack of a compatible fluorophore. Now this issue has been cleared up, measurements can be made with anionic surfactants and compared to the previous study.

Figure 5 (a) presents diameters of bubbles generated in different surfactant solutions. A slight decrease of the equivalent diameter of the bubble with the increase of surfactant concentration is observed in the presence of both the anionic surfactants studied. This decrease of diameter was due to the decrease of surface tension force during the bubble formation, which facilitated the detachment of bubbles. Velocities were also recorded and Figure 5 (b) presents the velocities of bubbles in different anionic surfactant solutions. A sharp decrease can be observed with increasing surfactant concentration. For the

STS (the surfactant with the longest chain) it occurred around 9.1×10^{-7} mol.L^{-1} and, for the shortest chain, SDS, this sharp decrease took place for a higher concentration, around 2.95×10^{-6} mol.L^{-1}. Such a decrease of velocity is characteristic of the contamination of the bubble by the surfactants.

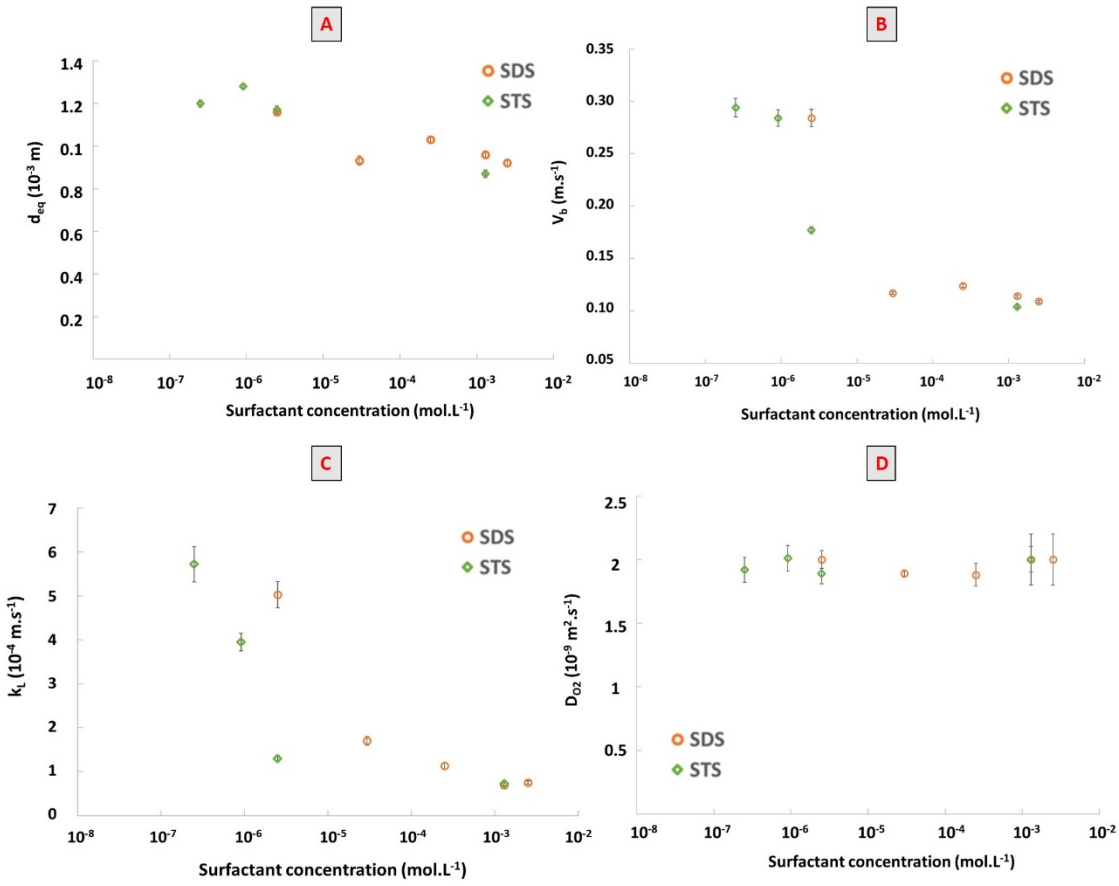

Figure 5: (a) Diameters (b) velocities (c) liquid side mass transfer coefficient and (d) oxygen diffusion coefficients measured in aqueous solutions of anionic surfactants.

Concerning the transfer from these bubbles, the mass transfer coefficients k_L measured in different surfactant solutions are presented in Figure 5 (c): the decrease of mass transfer with surfactant concentration is clearly highlighted and that at high concentration is about one tenth of the mass transfer at low concentration. Moreover, both surfactants reach the same extremely low value of k_L (0.7×10^{-4} m.s^{-1}) at the high concentration but, for intermediate concentrations, the surfactant with the longest chain (STS) is impacted at lower surfactant concentration than SDS, which has a shorter chain. This effect is the same as observed for the effect of hydrophobic chain length of cationic surfactants [48].

The diffusion coefficient of oxygen in the different surfactant solutions studied is plotted in Figure 5 (d). It can be observed that, in this range of concentrations, far from the interface, the diffusion coefficient of oxygen D_{O2} is not impacted by the presence of surfactant and keeps a value close to the one in water (around 2×10^{-9} $m^2.s^{-1}$).

3.3 Comparison with cationic and nonionic, modeling purpose

These new data on mass transfer from a single bubble rising in a solution containing anionic surfactant complement a previous study that considered cationic and nonionic surfactants. The data set obtained now covers the large diversity of surfactants and is big enough to propose some models. Current predicting models take the Schmidt number and the Reynolds number into account to predict the Sherwood number. It is shown in [37,42,57] that, for very concentrated solutions, the Frössling model, used for fully contaminated bubbles, overestimates the mass transfer. To explain the overestimation, the authors propose that another effect, taken into account neither by the Reynolds number nor by the Schmidt number in the bulk, inhibits mass transfer.

To show the effect of addition of surfactants on the Reynolds, Schmidt and Sherwood numbers, the ratio between the dimensionless number in the presence of surfactant and the one obtained in a pure solution has been calculated for all operating conditions. The θ_{cap} angle, calculated from the Sadhal & Johnson [8] model, describes the ratio for the bubble contaminated by surfactant. This contamination angle is calculated from a normalized drag coefficient C^*_D, presented in equation (6)

$$C_D^* = \frac{C_D - D_D^m}{C_D^{im} - C_D^m} = \frac{1}{2\pi}\left(2\left(\pi - \theta_{cap}\right) + \sin\left(\theta_{cap}\right) + \sin\left(2\theta_{cap}\right) - \frac{1}{3}\sin\left(3\theta_{cap}\right)\right) \quad (6)$$

where C_D is the experimental drag coefficient. C_D^{im} and C_D^m represent the drag coefficients of a fully contaminated and a clean bubble, respectively. These coefficients are calculated from the Schiller & Naumann correlation [58] (equation (7)) and Mei et al. correlation [59] (equation (8)).

$$C_D^{im} = \frac{24}{Re}(1 + 015Re^{0.687}) \quad (7)$$

$$C_D^m = \frac{16}{Re}\left(1 + \frac{Re}{8+0.5(Re+3.315Re^{0.5})}\right) \quad (8)$$

We will then use the coverage ratio R_{cap} calculated using equation (9).

$$R_{cap} = \frac{180-\theta_{cap}}{180} \quad (9)$$

The ratio is reported versus the coverage ratio R_{cap} in Figure 6.

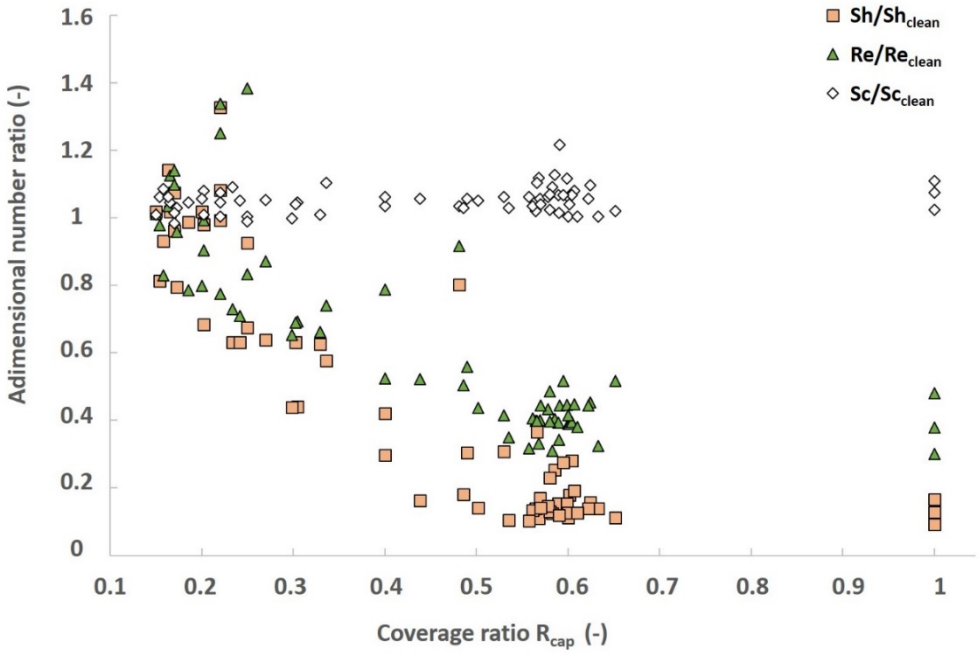

Figure 6: Comparison between Sherwood, Reynolds, and Schmidt numbers for clean and contaminated bubbles

It can be observed on Figure 6 that the Schmidt number is not significantly impacted by the increase of coverage ratio; the ratio of Schmidt numbers in the presence of surfactant to Schmidt number in pure water stays close to 1 even at high surface coverage. This makes sense, as the surfactant concentrations under test do not affect the diffusion coefficient (Figure 5(d)) nor the viscosity. The Reynolds number, however, is highly impacted by the presence of surfactant, as has already been highlighted by the study of the velocities (Figure 5(b)). The ratio decreases with increasing coverage ratio until it reaches a plateau, where the Reynolds number reaches around 30% of its value in clean water. With this in mind, it is obvious that the Reynolds number plays an important role in the decrease of mass transfer. However,

while the Reynolds number is decreased by around 70% by the presence of surfactant, the Sherwood number undergoes a greater decrease from a coverage ratio of 0.4, and the decrease in Sherwood number at high surface coverage is 15% greater than that in the Reynolds number.

Thus a large part of the decrease of Sherwood number is explained by the decrease of Reynolds number, but an additional effect would still be needed to explain why the Sherwood number is impacted 15% more than the Reynolds number.

To identify what parameter could be responsible for this additional effect, it is important to have a better view of the behavior of surfactants in the liquid phase and their affinity toward the interface. The "Sa" software [60] has been used to determine the adsorption parameters of SDS and STS according to the Frumkin isotherm [61] and the results, accompanied by previous ones on cationic and nonionic surfactants, are reported in Table 2. This software allows to fit experimental parameters with a solver baser on the Powell alogithm [62]. In the case of surface contamination, knowing that the surface tension is linked to the surface concentration according the Gibbs equation [63] :

$$\gamma = \gamma_0 + n_G RT\Gamma_\infty[\ln(1-\theta) + a_F\theta^2] \quad (10)$$

Where a_F (-) is a parameter that takes electrostatic interactions between surfactants into account and θ is the surface coverage, defined as the ratio between the surfactant concentration Γ (mol.m^{-2}) and the maximal surfactant concentration Γ_∞ (mol.m^{-2}). The adsorption parameters obtained are fitted from the Gibbs equation and the Langmuir [64] and Frumkin [61] isotherms presented in equations (11) and (12).

$$K_{LG}C = \frac{\theta}{1-\theta} \quad (11)$$

$$K_F C = \frac{\theta}{1-\theta}\exp(-2a_F\theta) \quad (12)$$

where C is the surfactant concentration (mol.m^{-3}), K_F and K_{LG} are the adsorption constants (m^3.mol^{-1}).

Kind of surfactant	Name	Frumkin K_F ($m^3.mol^{-1}$)	Langmuir K_{LG} ($m^3.mol^{-1}$)	a_F (-)	Γ_∞ (10^{-6} $m^2.mol^{-1}$)
Nonionic [48]	TX100	-	1053	-	2.76
	TX102	-	1194	-	2.43
	TX165	-	2240	-	1.90
	TX305	-	3294	-	1.36
Cationic [48]	C8TAC	0.02	-	0.04	2.43
	C12TAC	2.58	-	0.63	2.48
	C14TAC	1.05	-	0.91	2.60
	C16TAC	3.38	-	2.75	1.54
Anionic	SDS	0.43	-	1.37	3.55
	STS	0.72	-	2.73	2.48

Table 2: Constants of Frumkin and Langmuir adsorption isotherm for nonionic, cationic and anionic surfactants.

The results obtained for anionic surfactants show the same trend as cationic surfactant: the longer the hydrophobic chain, the lower the maximal surface concentration: 3.55×10^{-6} $mol.m^{-2}$ for SDS (the shortest chain), and 2.48×10^{-6} $mol.m^{-2}$ for STS (the longest chain). Moreover, this longer chain led to an adsorption at lower bulk concentrations. This effect is shown by the constant K_F. This value of K_F (and K_{LG} for nonionic surfactants, modelled by the Langmuir isotherm [64]) describes the equilibrium between surfactants in the liquid phase and at interface, according to the chemical equation :

$$S_{aq} + * \overset{K_F}{\Leftrightarrow} S_{ads}$$

where S_{aq} represents the number of surfactants in the liquid phase, * the number of vacant sites, and S_{ads} the number of surfactants adsorbed. In fact, if the constant K_F increases, the equilibrium is shifted toward the right (i.e., adsorbed surfactants).

For the following development, we note the adsorption constant as K, which represents K_{LG} for nonionic surfactants and K_F charged surfactants.

It has been suggested that the Sherwood number is not only impacted by the Schmidt and the Reynolds numbers, so, in this part, we chose to work with points that have the same Reynolds ($100<Re<107$) and Schmidt numbers ($500<Sc<562$). The corresponding Sherwood number varies between 98 and 30. This first observation again stresses that, for the same Schmidt and Reynolds conditions, the Sherwood number can vary by about 70%. The purpose is to find a third dimensionless number that could represent the additional impact of contamination on the mass transfer. The factor KC (adsorption constant and concentration, respectively in $m^3.mol^{-1}$ and $mol.m^{-1}$) seems to be a good candidate, since it represents the intrinsic adsorption properties of the surfactant and the state of the equilibrium between the bulk and the interface with bulk concentration. In order to take the electrostatic interactions into account, this dimensionless number can be divided by $\exp(-2a_F\theta)$. This term is present in the Frumkin isotherm and weights the equilibrium by taking electrostatic interactions into account. If interactions are neglected, as is the case for nonionic surfactants, the term a_F is equal to 0 and $\exp(-2a_F\theta)$ takes the value of 1 (i.e. does not impact KC). As a result, to take in account the previously mentioned parameters, the new dimensionless number should be $KC/\exp(-2a_F\theta)$.

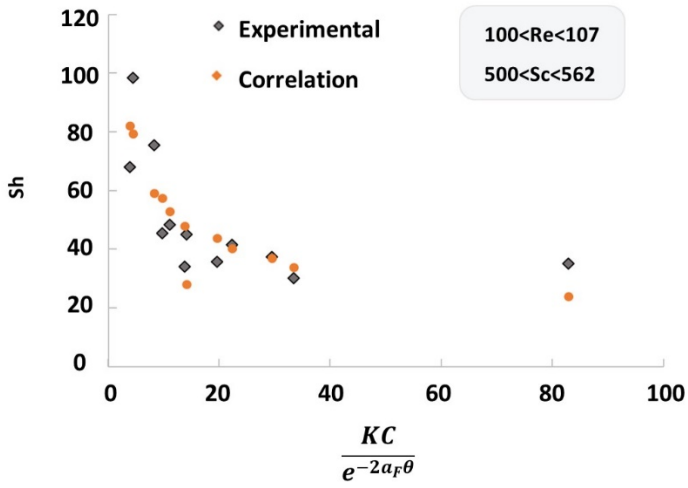

Figure 7: Variation of the Sherwood number according to KC/exp(-2a_Fθ) for the same range of Reynolds and Schmidt numbers

Figure 7 plots the Sherwood number against this new dimensionless number KC/exp(-2a_Fθ), for 100<Re<107 and 500<Sc<562. On this figure, we can observe that the Sherwood number undergoes a decrease when KC/exp(-2a_Fθ) increases. This means that, the more the equilibrium of surfactants between the bulk and the interface favors the adsorption (i.e., high KC/exp(-2a_Fθ)), the lower is the Sherwood number. To propose a model to fit these experimental points, we built our physical model using the scheme presented in Figure 8.

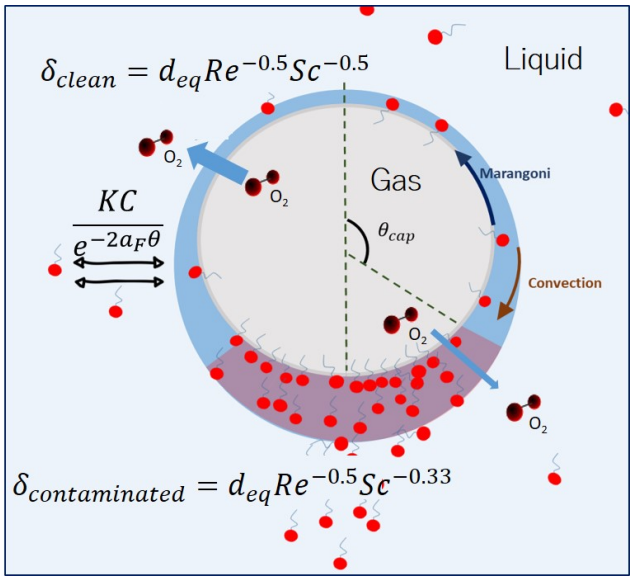

Figure 8: Scheme of the physical phenomenon occurring during the rise of a bubble in a liquid containing surfactants.

The bubble rises in the liquid containing surfactants. Surfactants are adsorbed and swept from the nose to the rear of the bubble because of convection as described in Palaparthi et al. [7]. As a result, the bubble can be split into two parts: the nose, almost clean of surfactant, and the rear, full of surfactants. The part covered by surfactant can be estimated by R_{cap} (cf. equation (9)). Therefore, the mean Sherwood number on the bubble is calculated from equation (13):

$$Sh_{correlated} = \left(1 - R_{cap}\right)Sh_{clean} + R_{cap}Sh_{contaminated} \tag{13}$$

By taking the third, previously mentioned, dimensionless number into account to model the effect of surfactant adsorption on the bubble we have:

$$Sh_{correlated} = \left(\left(1 - R_{cap}\right)Sh_{clean} + R_{cap}Sh_{contaminated}\right)\left(\frac{KC}{e^{-2a_F\theta}}\right)^{\psi} \tag{14}$$

where ψ is a constant that needs to be determined. The clean and contaminated Sherwood number can be calculated from the hydrodynamic thickness of each film and is expressed as equation (15).

$$Sh = \frac{d_{eq}k_L}{D_{O_2}} \tag{15}$$

The mass transfer coefficient of oxygen in the liquid side is

$$k_L = \frac{D_{O_2}}{\delta} \tag{16}$$

where δ is the thickness of the diffusion film. By combining (15) and (16):

$$Sh = \frac{d_{eq}}{\delta} \tag{17}$$

Finally, by replacing (17) in (14) the correlation becomes:

$$Sh_{correlated} = \left(R_{cap}\frac{d_{eq}}{\delta_{clean}} + \left(1 - R_{cap}\right)\frac{d_{eq}}{\delta_{contaminated}}\right)\left(\frac{KC}{e^{-2a_F\theta}}\right)^{\psi} \tag{18}$$

The thickness of each diffusion film is determined by the hydrodynamic conditions as equations (19) and (20) ([50] and [49]):

$$\delta_{clean} = d_{eq} Re^{-0.5} Sc^{-0.5} \quad (19)$$

$$\delta_{contaminated} = d_{eq} Re^{-0.5} Sc^{-0.33} \quad (20)$$

The solver of excel® was used to determine the value of ψ giving the best fit for the experimental points with this correlation, the method used were the least square method. The value converged toward -0.4 and the averaged deviation was about 20%. Figure 7 compares the experimental and correlated points. The correlated points follow the trend of experimental points well. The goal is thus to extend this correlation to all the experimental points. However, since the bubble is rising and undergoes convection, the amount of surfactants around the bubble will depend on (i) the convection, (ii) their adsorption kinetics. The contribution of the contamination term $KC/\exp(-2a_F\theta)$ to the Sherwood number will depend on these two parameters. In order to compare the effect of adsorption and convection, it is useful to calculate a scale, defined as:

$$\frac{convection\ effect}{contamination\ effect} = \frac{e^{-2a_F\theta} Re}{KC} \quad (21)$$

If this ratio is high, the convection is strong, and the effect of contamination can be neglected. When the ratio is weaker, contamination by surfactant takes on more importance. This ratio varies between 10^{-2} and 10^{6}. It was decided to split our results into 6 conditions for which Re and Sc are constant:

- Condition 1 : $\frac{convection\ effect}{contamination\ effect}$ [7.7×10^{6}-2.8×10^{5}]
- Condition 2 : $\frac{convection\ effect}{contamination\ effect}$ [2.0×10^{5}-6.6×10^{3}]
- Condition 3 : $\frac{convection\ effect}{contamination\ effect}$ [6.6×10^{3}-2.2×10^{2}]
- Condition 4 : $\frac{convection\ effect}{contamination\ effect}$ [2.2×10^{2}-2.7×10^{1}]
- Condition 5 : $\frac{convection\ effect}{contamination\ effect}$ [2.7×10^{1}-6.8×10^{-1}]

- Condition 6 : $\frac{convection\ effect}{contamination\ effect}$ [6.8×10^{-1}-4.5×10^{-2}]

The first condition then represents a situation where the convection outweighs the contamination by surfactants which can almost be neglected. Conversely, the 6th condition represents a major contamination, compared to the convection. Each regime contains around 10 experimental results (i.e., experiments on 60 bubbles). A value of ψ was determined for each regime (with excel® solver, least squared method). The value of ψ for each regime considered is supposed to represent the weighting of contamination effect of mass transfer. It is presented in Figure 9(a), in function of the ratio between convection and contaminaation. For a convection:contamination ratio lower than 100, ψ takes negative values and for ratios higher than 100 (i.e., convection preponderant) ψ takes positive values and tends toward 0.

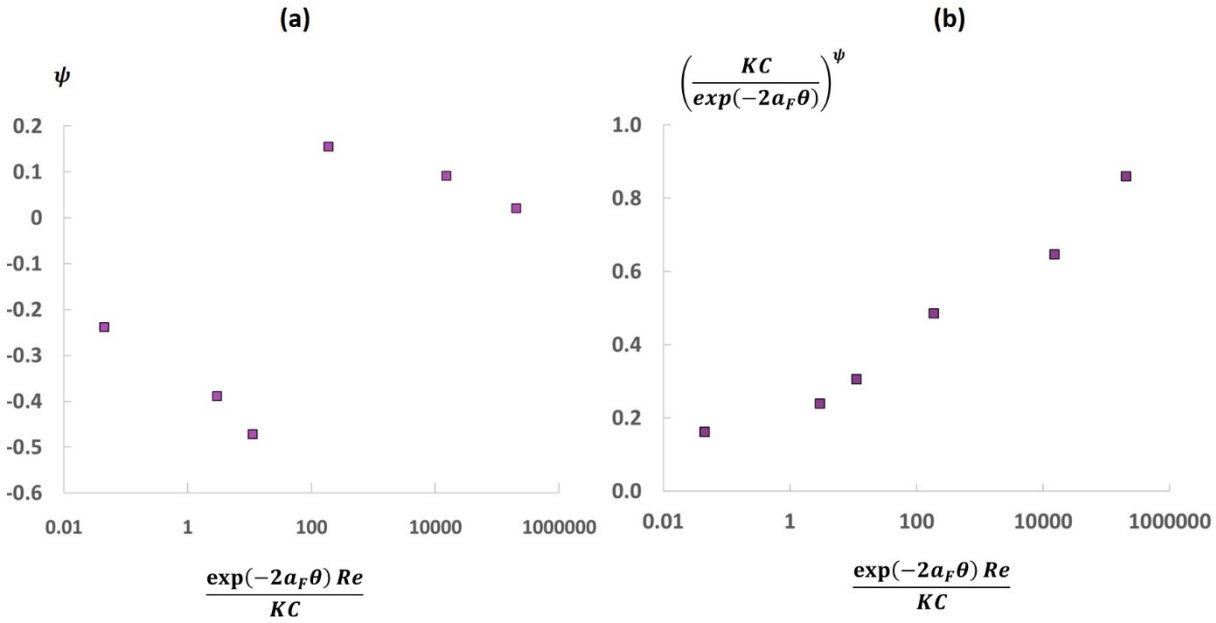

Figure 9: (a) Values of ψ obtained numerically according to the operating condition (b) Value of the corrective factor obtained according to the operating condition.

Although it can be surprising that ψ takes positive and negative value with a critical value at 100, it is important to keep in mind that it is a weighting parameter and to get the physical meaning of this term

it is demonstrated on the Figure 9(b), which represents the value of the correcting factor due to contamination, according to the regime. The correcting factor varies between 0 and 1 in an almost linear way. The more the value of the ratio increases, the closer the value of the contamination factor comes to 1 and, as a result, does not impact the value of $Sh_{correlated}$. Conversely, the low regimes (i.e. condition 5 and 6) , for which the contamination is high, have low values of the correcting factor, which means that the impact on the value of $Sh_{correlated}$ is strong.

The values of experimental and correlated Sherwood numbers for all our experimental points and also the point determined by Sardeing et al. [14] for small bubbles, are plotted versus the Reynolds number in Figure 10(a). They are also compared with the Frössling [50] and Higbie [49] correlations. The correlation seems to bring a good correction of Frössling and Higbie correlations to predict the Sherwood number for all Reynolds numbers studied, even for values that are lower than the Frössling prediction. The results extracted from Sardeing et al. are also well predicted by our correlation.

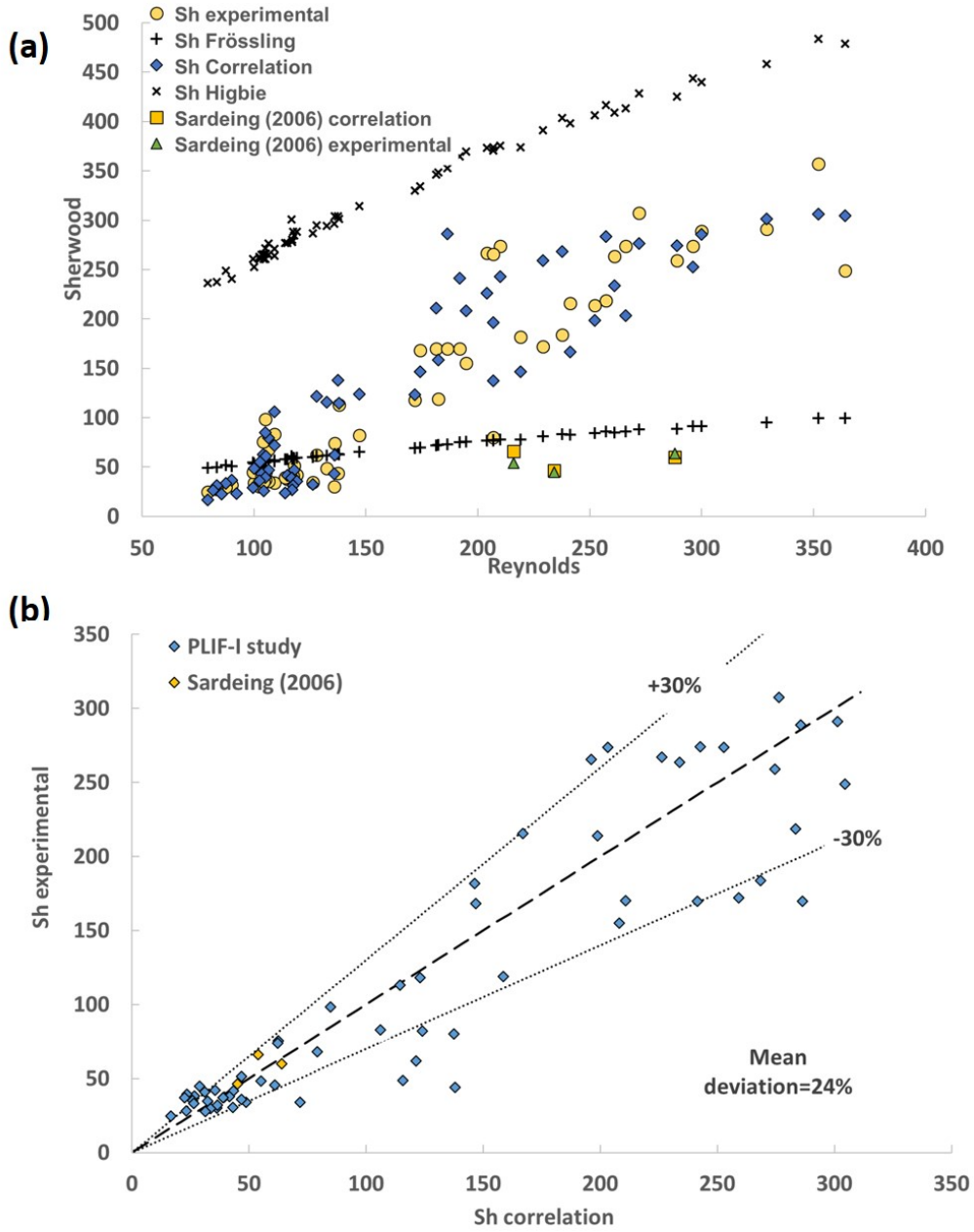

Figure 10: (a) Sherwood numbers of experimental results and correlations in function of the Reynolds number (b) Comparison between experimental points and correlation

In order to compare the experimental values of Sherwood number and the predictions of our correlation, the relation between the experimental and correlation Sherwood numbers is plotted in Figure 10(b). The mean deviation is 24%. The Sherwood numbers are well predicted by our correlation for the whole range of Sherwood numbers obtained experimentally. It seems that the correlation can slightly overestimate low Sherwood numbers and underestimate higher ones. This gap between the correlation and the model may be corrected with a better comparison between convection and contamination of the bubble. In order to compare the convection flux and the flux of surfactants contaminating the bubble in

a more rigorous way, we would need the diffusion coefficient of surfactants (D, $m^2.s^{-1}$), and the adsorption and desorption constants (k_a and k_d respectively in $m^3.mol^{-1}.s$ and s^{-1}). As described in Palaparthi et al. [7], the adsorption rate (kinetic rate) and the diffusive rate of surfactants may be compared with the convection rate to give information about the contamination state of the bubble, as proposed in equations (22) and (23):

$$\frac{diffusive\ rate}{convection\ rate} = \frac{k_d d_{eq}}{k_a 2\Gamma_\infty} Pe^{-0.5}\left(1 + \frac{k_a C}{k_d}\right) \quad (22)$$

$$\frac{kinetic\ rate}{convection\ rate} = \frac{k_d d_{eq}}{2V_b}\left(1 + \frac{k_a C}{k_d}\right) Pe^{-0.5} \quad (23)$$

where the Peclet number represents the ratio between the convective and the diffusive transport as $Pe=V_b d_{eq}/D$. However, accessing these parameters is not easy and requires additional experimentation, so this method would not be easily usable for industrial applications. The ratio representing the regime as it is presented in equation 12 can be used to calculate $Sh_{correlated}$ and gives an easy way to predict the mass transfer coefficient in the presence of surfactants, with an average error of 24%. This correlation gives interesting perspectives for its use in industrial application such as in wastewater treatment plants, and it would be interesting to investigate the use of this correlation in more complex media where rheology can as well impact the mass transfer [65–67].

4 Conclusion

In this paper, a luminescent probe $[Ru(dpp\text{-}diSO_3)_3]^{4-}$, has been synthetized in order to make measurement by Planar Laser Induced Fluorescence with Inhibition possible for the determination of oxygen mass transfer from a single isolated bubble in the presence of anionic molecules. In the first part, after a description of the synthesis protocol, the feasibility of using this fluorophore in PLIF-I experiments was checked, as was its performance in the presence of anionic surfactants. The fluorophore, $[Ru(dpp\text{-}diSO_3)_3]^4$, was found to be a very good oxygen sensor and compatible with anionic molecules. Then, thanks to its use, PLIF-I experiments were run with anionic surfactants: SDS and STS, at different bulk concentrations. These two surfactants were chosen because they both present the same

polar head, a sulfonate, and have linear chains with different numbers of carbons on their carbonated chain: 12 for SDS and 14 for STS. The study of hydrodynamic and mass transfer showed that mass transfer is highly impacted by the tail length of the anionic surfactant. The longer the hydrophobic chain is, the greater are the decreases in velocity and mass transfer, for a given bulk concentration. This effect is found to be the same as the effect of chain length variation found in our recent publication and can be explained by an equilibrium in favor of adsorption for lower bulk concentrations when the chain is longer and, as a result, the surfactant more hydrophobic.

Finally, the results of mass transfer measurement in the presence of anionic surfactants and the results of a previous study on cationic and nonionic surfactants have been compared with classical Higbie and Frössling correlations. The impact of modification of Reynolds and Schmidt numbers due to the presence of surfactants on the Sherwood number has been evaluated. It has been highlighted that, for every surfactant studied, the decrease of Reynolds and Schmidt numbers alone cannot explain the decrease of mass transfer at high surfactant contamination. A new correlation has been proposed, with a new dimensionless factor $KC/\exp(-2a_F\theta)$ that accounts for the effect of surfactants contamination. This factor represents the equilibrium between the adsorbed surfactants and the surfactant present in the bulk.

Promising perspectives for applications arise from this study, especially in wastewater treatment plants, where predicting the mass transfer coefficient is key to ensuring performance levels and energy preservation. With this in mind, it would be interesting to apply this model to a larger range of Reynolds numbers with a mix of contaminants, to approach industrial applications more closely. Moreover, it would be interesting to gain access to the diffusion coefficient, the adsorption, and the desorption constant of surfactants to check whether knowledge of these parameters leads to a better estimation of the contamination state of the bubble and so to a more accurate prediction of the mass transfer coefficient.

ACKNOWLEDGEMENT

The authors wish to thank the French National Research Agency (ANR) for the support received from the project MAMOTHS ANR-17-CE06-001.

References

[1] Roustan, M., 2003, *Transferts gaz-liquide dans les procédés de traitement des eaux et des effluents gazeux*, Tec & Doc Lavoisier, Paris.

[2] Treybal, R. E., 1955, *Mass-Transfer Operations*, McGraw-Hill.

[3] Gillot, S., Capela-Marsal, S., Roustan, M., and Héduit, A., 2005, "Predicting Oxygen Transfer of Fine Bubble Diffused Aeration Systems—Model Issued from Dimensional Analysis," Water Research, **39**(7), pp. 1379–1387.

[4] Clift, R., Grace, J. R., Weber, M. E., and Weber, M. F., 1978, *Bubbles, Drops, and Particles*, Academic Press.

[5] Guet, S., and Ooms, G., 2006, "Fluid Mechanical Aspects of the Gas-Lift Technique," Annual Review of Fluid Mechanics, **38**.

[6] Vázquez, G., Cancela, M. A., Riverol, C., Alvarez, E., and Navaza, J. M., 2000, "Application of the Danckwerts Method in a Bubble Column: Effects of Surfactants on Mass Transfer Coefficient and Interfacial Area," Chemical Engineering Journal, **78**(1), pp. 13–19.

[7] Palaparthi, R., Papageorgiou, D., and Maldarelli, C., 2006, "Theory and Experiments on the Stagnant Cap Regime in the Motion of Spherical Surfactant-Laden Bubbles," Journal of Fluid Mechanics, **559**, pp. 1–44.

[8] Sadhal, S. S., and Johnson, R. E., 1983, "Stokes flow past bubbles and drops partially coated with thin films. Part 1. Stagnant cap of surfactant film – exact solution," Journal of Fluid Mechanics, **126**, pp. 237–250.

[9] Gómez-Díaz, D., Navaza, J. M., and Sanjurjo, B., 2009, "Mass-Transfer Enhancement or Reduction by Surfactant Presence at a Gas−Liquid Interface," Industrial & Engineering Chemistry Research, **48**(5), pp. 2671–2677.

[10] Álvarez, E., Gómez-Díaz, D., Navaza, J. M., and Sanjurjo, B., 2008, "Continuous Removal of Carbon Dioxide by Absorption Employing a Bubble Column," Chemical Engineering Journal, **137**(2), pp. 251–256.

[11] Bouaifi, M., Hebrard, G., Bastoul, D., and Roustan, M., 2001, "A Comparative Study of Gas Hold-up, Bubble Size, Interfacial Area and Mass Transfer Coefficients in Stirred Gas–Liquid Reactors and Bubble Columns," Chemical Engineering and Processing: Process Intensification, **40**(2), pp. 97–111.

[12] Cockx, A., Roustan, M., Line, A., and Hébrard, G., 1995, "Modeling of Mass-Transfer Coefficient K-L in Bubble-Columns," Chemical Engineering Research and Design, **73**(6), pp. 627–631.

[13] Hebrard, G., Zeng, J., and Loubiere, K., 2009, "Effect of Surfactants on Liquid Side Mass Transfer Coefficients: A New Insight," Chemical Engineering Journal, **148**(1), pp. 132–138.

[14] Sardeing, R., Painmanakul, P., and Hébrard, G., 2006, “Effect of Surfactants on Liquid-Side Mass Transfer Coefficients in Gas–Liquid Systems: A First Step to Modeling,” Chemical Engineering Science, **61**(19), pp. 6249–6260.

[15] Vasconcelos, J. M. T., Orvalho, S. P., and Alves, S. S., 2002, “Gas–Liquid Mass Transfer to Single Bubbles: Effect of Surface Contamination,” American Institute of Chemical Engineers Journal, **48**(6), pp. 1145–1154.

[16] Ahmia, A., Idouhar, M., Wongwailikit, K., Dietrich, N., and Hébrard, G., 2019, “Impact of Cellulose and Surfactants on Mass Transfer of Bubble Columns,” Chemical Engineering & Technology, **42**.

[17] Painmanakul, P., Loubière, K., Hébrard, G., Mietton-Peuchot, M., and Roustan, M., 2005, “Effect of Surfactants on Liquid Side Mass Transfer Coefficient,” Chemical Engineering Science, **60**, pp. 6480–6491.

[18] Deising, D., Bothe, D., and Marschall, H., 2018, “Direct Numerical Simulation of Mass Transfer in Bubbly Flows,” Computers & Fluids, **172**, pp. 524–537.

[19] Pesci, C., Weiner, A., Marschall, H., and Bothe, D., 2018, “Computational Analysis of Single Rising Bubbles Influenced by Soluble Surfactant,” Journal of Fluid Mechanics, **856**, pp. 709–763.

[20] Weiner, A., Timmermann, J., Pesci, C., Grewe, J., Hoffmann, M., Schlüter, M., and Bothe, D., 2019, “Experimental and Numerical Investigation of Reactive Species Transport around a Small Rising Bubble,” Chemical Engineering Science: X, **1**, p. 100007.

[21] Dani, A., Cockx, A., Legendre, D., and Guiraud, P., 2022, “Effect of Spheroid Bubble Interface Contamination on Gas-Liquid Mass Transfer at Intermediate Reynolds Numbers: From DNS to Sherwood Numbers,” Chemical Engineering Science, **248**, p. 116979.

[22] Wolff, L. M., Liu, Z.-C., and Hanratty, T. J., 1991, “A Fluorescence Technique to Measure Concentration Gradients near an Interface,” ASCE, pp. 210–218.

[23] Wolff, L. M., and Hanratty, T. J., 1994, “Instantaneous Concentration Profiles of Oxygen Accompanying Absorption in a Stratified Flow,” Experiments in Fluids, **16**(6), pp. 385–392.

[24] Woodrow, P. T., and Duke, S. R., 2001, “Laser-Induced Fluorescence Studies of Oxygen Transfer Across Unsheared Flat and Wavy Air−Water Interfaces,” Industrial & Engineering Chemistry Research, **40**(8), pp. 1985–1995.

[25] Butler, C., Cid, E., and Billet, A.-M., 2016, “Modelling of Mass Transfer in Taylor Flow: Investigation with the PLIF-I Technique,” Chemical Engineering Research and Design, **115, Part B**, pp. 292–302.

[26] Roudet, M., Loubiere, K., Gourdon, C., and Cabassud, M., 2011, “Hydrodynamic and Mass Transfer in Inertial Gas–Liquid Flow Regimes through Straight and Meandering Millimetric Square Channels,” Chemical Engineering Science, **66**(13), pp. 2974–2990.

[27] Roudet, M., Billet, A.-M., Cazin, S., Risso, F., and Roig, V., 2017, “Experimental Investigation of Interfacial Mass Transfer Mechanisms for a Confined High-Reynolds-Number Bubble Rising in a Thin Gap,” American Institute of Chemical Engineers Journal, **63**(6), pp. 2394–2408.

[28] Bork, O., Schlueter, M., and Raebiger, N., 2005, “The Impact of Local Phenomena on Mass Transfer in Gas-Liquid Systems,” The Canadian Journal of Chemical Engineering, **83**(4), pp. 658–666.

[29] Hiby, J. W., Braun, D., and Eickel, K. H., 1967, “Eine Fluoreszenzmethode zur Untersuchung des Stoffübergangs bei der Gasabsorption im Rieselfilm,” Chemie Ingenieur Technik, **39**(5–6), pp. 297–301.

[30] Huang, J., and Saito, T., 2017, “Influences of Gas–Liquid Interface Contamination on Bubble Motions, Bubble Wakes, and Instantaneous Mass Transfer,” Chemical Engineering Science, **157**, pp. 182–199.

[31] Kong, G., Buist, K. A., Peters, E. A. J. F., and Kuipers, J. A. M., 2018, “Dual Emission LIF Technique for PH and Concentration Field Measurement around a Rising Bubble,” Experimental Thermal and Fluid Science, **93**, pp. 186–194.

[32] Kováts, P., Thévenin, D., and Zähringer, K., 2020, “Influence of Viscosity and Surface Tension on Bubble Dynamics and Mass Transfer in a Model Bubble Column,” International Journal of Multiphase Flow, **123**, p. 103174.

[33] Lacassagne, T., Simoëns, S., El Hajem, M., and Champagne, J.-Y., 2018, “Ratiometric, Single-Dye, PH-Sensitive Inhibited Laser-Induced Fluorescence for the Characterization of Mixing and Mass Transfer,” Experiments in Fluids, **59**(1), p. 21.

[34] Someya, S., Bando, S., Song, Y., Chen, B., and Nishio, M., 2005, “DeLIF Measurement of PH Distribution around Dissolving CO2 Droplet in High Pressure Vessel,” International Journal of Heat and Mass Transfer, **48**(12), pp. 2508–2515.

[35] Stöhr, M., Schanze, J., and Khalili, A., 2009, “Visualization of Gas–Liquid Mass Transfer and Wake Structure of Rising Bubbles Using PH-Sensitive PLIF,” Experiments in Fluids, **47**(1), pp. 135–143.

[36] Valiorgue, P., Souzy, N., Hajem, M. E., Hadid, H. B., and Simoëns, S., 2013, “Concentration Measurement in the Wake of a Free Rising Bubble Using Planar Laser-Induced Fluorescence (PLIF) with a Calibration Taking into Account Fluorescence Extinction Variations,” Experiments in Fluids, **54**(4), p. 1501.

[37] Jimenez, M., Dietrich, N., Grace, J. R., and Hébrard, G., 2014, “Oxygen Mass Transfer and Hydrodynamic Behaviour in Wastewater: Determination of Local Impact of Surfactants by Visualization Techniques,” Water Research, **58**, pp. 111–121.

[38] Francois, J., Dietrich, N., Guiraud, P., and Cockx, A., 2011, “Direct Measurement of Mass Transfer around a Single Bubble by Micro-PLIFI,” Chemical Engineering Science, **66**(14), pp. 3328–3338.

[39] Dani, A., Guiraud, P., and Cockx, A., 2007, “Local Measurement of Oxygen Transfer around a Single Bubble by Planar Laser-Induced Fluorescence,” Chemical Engineering Science, **62**(24), pp. 7245–7252.

[40] Xu, F., Jimenez, M., Dietrich, N., and Hébrard, G., 2017, "Fast Determination of Gas-Liquid Diffusion Coefficient by an Innovative Double Approach," Chemical Engineering Science, **170**, pp.68-76.

[41] Xu, F., Cockx, A., Hébrard, G., and Dietrich, N., 2018, "Mass Transfer and Diffusion of a Single Bubble Rising in Polymer Solutions," Industrial & Engineering Chemistry Research, **57**(44), pp. 15181–15194.

[42] Lebrun, G., Xu, F., Le Men, C., Hébrard, G., and Dietrich, N., 2021, "Gas–Liquid Mass Transfer around a Rising Bubble: Combined Effect of Rheology and Surfactant," Fluids, **6**(2), p. 84.

[43] Jimenez, M., Dietrich, N., and Hébrard, G., 2013, "Mass Transfer in the Wake of Non-Spherical Air Bubbles Quantified by Quenching of Fluorescence," Chemical Engineering Science, **100**, pp. 160–171.

[44] Jia, X., Hu, W., Yuan, X., and Yu, K., 2015, "Effect of Surfactant Type on Interfacial Area and Liquid Mass Transfer for CO2 Absorption in a Bubble Column," Chinese Journal of Chemical Engineering, **23**(3), pp. 476–481.

[45] Orhan, R., and Dursun, G., 2016, "Effects of Surfactants on Hydrodynamics and Mass Transfer in a Co-Current Downflow Contacting Column," Chemical Engineering Research and Design, **109**, pp. 477–485.

[46] Chen, X., Liu, G., Fan, H., Li, M., Luo, T., Qi, L., and Wang, H., 2013, "Effects of Surfactant Contamination on Oxygen Mass Transfer in Fine Bubble Aeration Process," Korean Journal of Chemical Engineering, **30**(9), pp. 1741–1746.

[47] García-Abuín, A., Gómez-Díaz, D., Navaza, J. M., and Sanjurjo, B., 2010, "Effect of Surfactant Nature upon Absorption in a Bubble Column," Chemical Engineering Science, **65**(15), pp. 4484–4490.

[48] Lebrun, G., Benaissa, S., Le Men, C., Pimienta, V., Hébrard, G., and Dietrich, N., 2022, "Effect of Surfactant Lengths on Gas-Liquid Oxygen Mass Transfer from a Single Rising Bubble," Chemical Engineering Science, **247**, p. 117102.

[49] Higbie, R., 1935, *The Rate of Absorption of a Pure Gas into Still Liquid during Short Periods of Exposure*, New York.

[50] Frössling, N., 1938, "Uber Die Verdunstung Fallender Tropfen," Beiträge zur Geophysok Gerlands, **52**, pp. 170–216.

[51] du Noüy, P. L., 1925, "An interfacial tensiometer for universal use", Journal of General Physiology, **7**(5), pp. 625–631.

[52] Castellano, F. N., and Lakowicz, J. R., 1998, "A Water-Soluble Luminescence Oxygen Sensor," Photochemistry and Photobiology, **67**(2), pp. 179–183.

[53] Babak, M. V., Faouder, P. L., Trivelli, X., Venkatesan, G., Bezzubov, S. I., Kajjout, M., Gushchin, A. L., Hanif, M., Poizat, O., Vezin, H., and Rolando, C., 2020, "Heteroleptic Ruthenium(II) Complexes with Bathophenanthroline and Bathophenanthroline Disulfonate Disodium Salt as Fluorescent Dyes for In-Gel Protein Staining," Inorganic Chemistry, **59**(7), pp.4527-4535.

[54] Beves, J. E., Constable, E. C., Housecroft, C. E., Neuburger, M., Schaffner, S., and Zampese, J. A., 2008, "4′-Chloro-2,2′:6′,2″-Terpyridine (L): Ethyl Sulfate Salts of $[H_2L]^{2+}$ and the Single Crystal Structures of $[H_2L][EtOSO_3]Cl \cdot H_2O$ and $[ML_2][PF_6]_2$ with M=Fe and Ru," Inorganic Chemistry Communications, **11**(9), pp. 1006–1008.

[55] Luis, E. T., Ball, G. E., Gilbert, A., Iranmanesh, H., Newdick, C. W., and Beves, J. E., 2016, "Efficient Microwave-Assisted Synthesis and Characterization of Key Ruthenium(II) Polypyridyl Complexes $[Ru(Bpy)_3](PF_6)_2$, $[Ru(Phen)_3](PF_6)_2$, $[Ru(Bpy)_3(Phen)](PF_6)_2$ and $[Ru(Phen)_2(Bpy)](PF_6)_2$," Journal of Coordination Chemistry, **69**(11–13), pp. 1686–1694.

[56] Dietrich, N., Francois, J., Jimenez, M., Cockx, A., Guiraud, P., and Hébrard, G., 2015, "Fast Measurements of the Gas-Liquid Diffusion Coefficient in the Gaussian Wake of a Spherical Bubble," Chemical Engineering & Technology, **38**(5), pp. 941–946.

[57] Jimenez, M., 2013, "Etude Du Transfert de Matière Gaz/Liquide En Milieux Complexes: Quantification Du Transfert d'oxygène Par Techniques Optiques," PhD thesis, INSA Toulouse, France.

[58] Schiller, L., and Naumann, A. Z., 1933, "Ueber Die Grundlegenden Berechnungen Bei Der Schwerkraftaufbereitung," Zeitschrift des Vereines Deutscher Ingenieure, **77**, pp. 318–321.

[59] Mei, R., Klausner, J. F., and Lawrence, C. J., 1994, "A Note on the History Force on a Spherical Bubble at Finite Reynolds Number," Physics of Fluids, **6**(1), pp. 418–420.

[60] *Http://Cinet.Chim.Pagesperso-Orange.Fr/Tele_sa/Install_Sa_Eng.Html*.

[61] Frumkin, A., 1925, "Die Kapillarkurve Der Höheren Fettsäuren Und Die Zustandsgleichung Der Oberflächenschicht," Zeitschrift für Physikalische Chemie, **116U**(1), pp. 466–484.

[62] Powell, M.J.D., 1964, "An efficient method for finding the minimum of a function of several variables without calculating derivatives", The Computer Journal, **7**(2), pp. 155-162.

[63] Gibbs, J.W., 1874, "On the equilibrium of heterogeneous substances", Connecticut Academy of Arts and Science.

[64] Langmuir, I., 1917, "The constitution and fundamental properties of solids and liquids II. Liquids.1" Journal of the American Chemical Society, **39**(9), pp. 1848–1906.

[65] Bajón Fernández, Y., Cartmell, E., Soares, A., McAdam, E., Vale, P., Darche-Dugaret, C., and Jefferson, B., 2015, "Gas to Liquid Mass Transfer in Rheologically Complex Fluids," Chemical Engineering Journal, **273**, pp. 656–667.

[66] García-Abuín, A., Gómez-Díaz, D., Losada, M., and Navaza, J. M., 2013, "Oxygen Absorption in Polymer+surfactant Aqueous Solutions," Chemical Engineering Journal, **225**, pp. 76–83.

[67] Jamnongwong, M., Loubiere, K., Dietrich, N., and Hébrard, G., 2010, "Experimental Study of Oxygen Diffusion Coefficients in Clean Water Containing Salt, Glucose or Surfactant: Consequences on the Liquid-Side Mass Transfer Coefficients," Chemical Engineering Journal, **165**(3), pp. 758–768.

SUPPLEMENTARY MATERIAL

Evaluation of errors:

Velocity

$$\frac{\Delta V_b}{V_b} = \frac{2}{number\ of\ images\ \sqrt{3}}$$

(the number of images is comprises between 40 and 100)

Diameter

$$\frac{\Delta d_{eq}}{d_{eq}} = \sqrt{\left(\frac{2\Delta a}{3a}\right)^2 + \left(\frac{\Delta b}{3b}\right)^2}$$

(with a and b repectively the big and small diameters of the bubble. Δa and Δb are calculated from the sampling of the camera, we consider an uncertainty of 1 pixel = 20,31 μm)

Integral of oxygen concentration

$$\iint [O_2](x,y)dxdy \ \ in\ noted\ m_{O2}$$

$$\frac{\Delta m_{O2}}{m_{O2}} = \sqrt{\left(\frac{\Delta M_{O2}}{M_{O2}}\right)^2 + \left(\frac{\Delta \delta_{camera}}{\delta_{camera}}\right)^2}$$

(With M_{O2} the dispersion on all values of the integral during the measurement (always <5%) and δ_{camera} is the uncertainty given by the sampling of the camera (4.37 μm))

Mass transfer coefficient

$$\frac{\Delta k_L}{k_L} = \sqrt{\left(\frac{\Delta m_{O2}}{m_{O2}}\right)^2 + 4\left(\frac{\Delta d_{eq}}{d_{eq}}\right) + \left(\frac{\Delta V_b}{V_b}\right)^2 + \left(\frac{\Delta[O_2]}{([O_2]^* - [O_2]_0)}\right)}$$

(with $\Delta[O_2]$ given by the oxygen probe ±0.02 mg/L)

It has to be noted that each measurement has been run 6 times to ensure the repeatability of measurements. The dispersion of results was always found to be closed to $\frac{\Delta k_L}{k_L}$.

Diffusion coefficient

The diffusion coefficient is calculated with a correlation coefficient higher than 97%, this suggest that the measured uncertainties are lower than the relative standard deviation. The error bar given on experimental results are then the standard deviation.

SDS					
Concentration (mol/L)	1.3×10^{-3}	2.5×10^{-3}	2.5×10^{-4}	2.95×10^{-5}	2.5×10^{-6}
Bubble velocity (10^{-3} m/s)	114±1	109±1	124±2	117±1	284±8
Bubble diameter (10^{-3} m)	0.96±0.02	0.92±0.02	1.03±0.02	0.93±0.02	1.16±0.02
Equilibrium surface tension (10^{-3} N/m)	52±1	44±1	68±1	71±1	71±1
Integral of oxygen concentration field (10^{-5} mg/m)	1.60±0.08	1.65±0.08	2.8±0.1	3.5±0.2	6.8±0.3
Oxygen diffusion coefficient (10^{-9} m^2/s)	2.0±0.1	2.0±0.2	1.9±0.1	1.89±0.03	2.00±0.07
Mass transfer coefficient (10^{-4} m/s)	0.70±0.04	0.75±0.04	1.13±0.07	1.7±0.1	5.0±0.3
Relative standard deviation of mass transfer coefficient	0.07	0.03	0.03	0.05	0.06
Schmidt number	500±25	500±50	532±16	529±8	500±17
Reynolds number	109±3	100±2	128±3	109±3	329±11
Sherwood number	34±2	34±4	62±4	83±4	291±11

STS				
Concentration (mol/L)	1.3×10^{-3}	2.5×10^{-6}	9.1×10^{-7}	2.5×10^{-7}
Bubble velocity (10^{-3} m/s)	104±1	177±3	284±8	294±9
Bubble diameter (10^{-3} m)	0.87±0.02	1.17±0.02	1.28±0.02	1.20±0.02
Equilibrium surface tension (10^{-3} N/m)	40±1	71±1	71±1	70±1
Integral of oxygen concentration field (10^{-5} mg/m)	1.47±0.07	2.9±0.1	6.3±0.3	8.0±0.4
Oxygen diffusion coefficient (10^{-9} m^2/s)	2.0±0.2	1.89±0.08	2.0±0.1	1.9±0.1
Mass transfer coefficient (10^{-4} m/s)	0.73±0.04	1.20±0.07	3.9±0.2	5.7±0.4
Relative standard deviation of mass transfer coefficient	0.05	0.05	0.03	0.05
Schmidt number	505±51	529±22	493±24	521±27
Reynolds number	90±2	207±5	364±11	352±12
Sherwood number	32±3	80±4	249±13	357±20